Control of out-of-plane anti-damping spin torque with a canted ferromagnetic spin source

Xiaoxi Huang[1,11,*], Daniel A. Pharis[1,11], Hang Zhou[2], Zishen Tian[3,8], Thow Min Jerald Cham[1], Kyoungjun Lee[4], Yilin Evan Li[5], Chaoyang Wang[6], Yuhan Liang[1], Maciej Olszewski[1], Di Yi[6], Chang-Beom Eom[4], Darrell G. Schlom[5,7,10], Lane W. Martin[3,8,9], Ding-Fu Shao[2], and Daniel C. Ralph[1,7,*]

[1]Department of Physics, Cornell University, Ithaca, NY 14853, USA
[2]Key Laboratory of Materials Physics, Institute of Solid-State Physics, HFIPS, Chinese Academy of Sciences, Hefei 230031, China
[3]Department of Materials Science and Engineering, University of California, Berkeley, CA 94720, USA
[4]Department of Materials Science and Engineering, University of Wisconsin-Madison, Wisconsin 53706, USA
[5]Department of Materials Science and Engineering, Cornell University, Ithaca, NY 14853, USA
[6]State Key Laboratory of New Ceramics and Fine Processing, School of Materials Science and Engineering, Tsinghua University, Beijing 100084, China
[7]Kavli Institute at Cornell for Nanoscale Science, Ithaca, NY 14853, USA
[8]Rice Advanced Materials Institute, Rice University, Houston, TX 77005, USA
[9]Department of Materials Science and NanoEngineering, Chemistry, and Physics and Astonomy, Rice University, Houston, TX 77005, USA
[10]Leibniz-Institut für Kristallzüchtung, Max-Born-Str. 2, 12489 Berlin, Germany
[11]These authors contributed equally: Xiaoxi Huang, Daniel A. Pharis

To achieve efficient anti-damping switching of nanoscale magnetic memories with perpendicular magnetic anisotropy using spin-orbit torque requires that the anti-damping spin-orbit torque have a strong out-of-plane component. The spin anomalous Hall effect and the planar Hall effect spin current produced by a ferromagnetic layer are candidate mechanisms for producing such an out-of-plane anti-damping torque, but both require that the magnetic moment of the spin source layer be canted partly out of the sample plane at zero applied magnetic field. Here we demonstrate such a canted configuration for a ferromagnetic $SrRuO_3$ layer and we characterize all vector components of the torque that it produces,

* E-mail: xh384@cornell.edu, dcr14@cornell.edu

including non-zero out-of-plane anti-damping torques. We verify that the out-of-plane spin component can be tuned by the orientation of magnetic moment, with significant contributions from both the spin anomalous Hall effect and the planar Hall effect spin current.

High-density magnetic random access memory (MRAM), which for thermal stability must be based on magnetic layers with perpendicular magnetic anisotropy (PMA), is attractive for its natural non-volatility and excellent endurance as compared to competing technologies [1, 2]. Anti-damping spin-orbit torque exerted by spin currents generated within materials having strong spin-orbit interactions is a leading candidate for enhancing the write efficiency in such memories to make them competitive for energy-constrained applications [3–12]. Unfortunately, spin-source materials with high symmetry can only produce anti-damping spin-orbit torque with orientation within the sample plane, which means that they are not capable of driving efficient anti-damping switching of nanoscale PMA magnets [13, 14]. Efficient switching of nanoscale PMA magnets by anti-damping spin-orbit-torque requires spin-source materials in which the symmetry constraints are relaxed either by a low-symmetry crystal structure [15–19] or magnetic order [20–26], to allow a component of out-of-plane anti-damping torque. Modeling suggests that an out-of-plane damping-like torque efficiency $\xi^Z_{DL} \approx 0.05$ is necessary for spin-orbit-torque MRAM to achieve energy efficiency better than conventional spin-transfer-torque MRAM for 40 nm devices, while $\xi^Z_{DL} \approx 0.30$ would allow better energy efficiency even than volatile SRAM with a much more compact circuit geometry [27]. Research on developing spin-source materials for out-of-plane anti-damping torque has so far fallen short of these thresholds, except for perhaps the low-symmetry van der Waals semimetal $TaIrTe_4$, for which recent studies report conflicting results [18, 28, 29]. Nonetheless, generating out-of-plane anti-damping torque with $TaIrTe_4$ requires domain-free flakes completely free of monolayer steps, so $TaIrTe_4$ is unlikely to be a solution for a manufacturable technology.

Here we pursue the strategy of generating an out-of-plane anti-damping torque with a ferromagnetic spin source layer in which the orientation of the ferromagnetic moment provides the required symmetry breaking. Several mechanisms have been proposed and demonstrated with initial experiments for how ferromagnets may be used as a source of spin current with a spin orientation that is controllable by changing the magnetization direction [30, 31]: e.g., via the spin anomalous Hall effect (AHE) [20, 22, 32, 33], the planar Hall effect (PHE) spin current [20, 34, 35], or spin rotation or spin swapping at a magnetic interface [36–40]. Initial experiments suggest that the spin AHE and the PHE spin current are particularly promising. To generate a vertically flowing spin current with an out-of-plane spin component via either of these mechanisms requires that the magnetization of the spin-source layer be canted partially out of the sample plane (i.e., neither fully in the sample plane nor fully perpendicular to the plane): the out-of-plane anti-damping torque due to the spin AHE is predicted to be proportional to $m_Y m_Z$ and that due to the PHE spin-current mechanism is predicted to be proportional to $m_X m_Z^2$ [20]. (Here $\hat{m}$ is the magnetic orientation, $\hat{X}$ is the direction of the in-plane applied charge current, and $\hat{Z}$ is perpendicular to the sample plane.) The strength of the underlying physical mechanisms for both the spin AHE and PHE spin currents have been measured previously using samples with either in-plane magnetizations [22, 32] or with magnets canted using large saturating magnetic fields [33–35], with efficiencies as large as $\xi_{DL}^{Y} = 0.25$ for the in-plane torque efficiency generated by in-plane-magnetized $L1_0$ FePt [32] via the spin AHE. The challenge with using these mechanisms to generate out-of-plane anti-damping torque for practical applications is to stabilize a partially-canted magnetic configuration with zero applied magnetic field. Thin-film samples governed entirely by shape anisotropy and first-order interfacial anisotropy have either purely in-plane or PMA configurations, so to have a stable partially-canted magnetic configuration requires use of magneto-crystalline anisotropy.

In a high-crystal-symmetry non-magnetic spin source material, an electric-field induced spin current that flows vertically can have a spin polarization only in an in-plane direction orthogonal to both the electric field and spin current (Fig. 1a). Fortunately, this constraint can be relaxed if the spin-source material has magnetic order. The electric-field generated spin current produced by a ferromagnetic spin-source layer can have a part with the symmetry of the conventional in-plane spin-orbit torque that does not depend on the magnetization direction (Fig. 1a) plus a part that does depend on the magnetization direction [30]. The geometries of the magnetization-dependent spin currents generated by the PHE and AHE [20] are shown in Fig. 1b,c for two different orientations of the canted magnetization relative to an applied electric field, $\vec{E}$. Both the PHE and AHE give rise to spin currents with their spin polarization aligned with magnetization of the spin-source layer, but with different flow directions: for the PHE spin current the flow is parallel to $\hat{m}(\hat{m} \cdot \vec{E})$ (Fig. 1b) and for the spin AHE the flow is along $\hat{m} \times \vec{E}$ (Fig. 1c). To achieve a vertically flowing spin current with an out-of-plane spin component, therefore, the PHE can contribute when the magnetization has a canted component in the $\hat{X}$-$\hat{Z}$ plane, and the AHE can similarly contribute when the magnetization has a canted component in the $\hat{Y}$-$\hat{Z}$ plane. As a function of the angle ψ of the applied electric field relative to the projection of the canted magnetization onto the sample plane, this means that the out-of-plane anti-damping torque should have a $\cos(\psi)$ dependence for the PHE spin current and a $\sin(\psi)$ dependence for the spin AHE. These results can be generalized: based on a symmetry analysis any time-reversal-odd spin current contributing to an out-of-plane anti-damping torque should give a $\cos(\psi)$ dependence, and any time-reversal-even spin current should give a $\sin(\psi)$ dependence (see Supplementary Information Section 5).

To achieve a magnetic spin-source layer with a partially-canted magnetization at zero applied magnetic field, we employ $SrRuO_3$ as the spin source [41–43] and deposit it on vicinal (001)-oriented $SrTiO_3$ substrates with a miscut angle around 0.1° and a miscut direction close to [010] (Methods). $SrRuO_3$ is an itinerant ferromagnet with a bulk Curie temperature $T_C \sim 160$ K [44, 45] and an orthorhombic crystal structure with lattice parameters $a_o = 5.5670$ $\mathring{A}$, $b_o = 5.5304$ $\mathring{A}$, and $c_o = 7.8446$ $\mathring{A}$ (the subscript o denotes orthorhombic structure) [46]. In the bulk, the magnetic easy axis aligns with $[010]_o$, which we will call the b axis [47], with a large magnetocrystalline anisotropy field, ~ 12 T [48]. When deposited on cubic, well-oriented (001)-$SrTiO_3$ substrates, $SrRuO_3$ thin films can grow epitaxially with six different domain configurations (see Supplementary Information Section 1). Nevertheless, by nucleating growth from step edges on a vicinal substrate, a single domain can be made dominant [49, 50]. With this method we achieve the predominant epitaxial configuration shown schematically in Fig. 2a, a $(110)_o$-oriented $SrRuO_3$ film with $SrRuO_3$ $[110]_o \parallel$ $SrTiO_3$ [001], $SrRuO_3$ $[001]_o \parallel$ STO [010], and $SrRuO_3$ $[\bar{1}10]_o \parallel$ STO [100], resulting in the bulk magnetic easy axis (i.e., the b axis) canted uniformly away from the surface normal [47]. We verified this growth orientation using x-ray diffraction with reciprocal space mapping (Supplementary Information Section 1). Unsuccessful growths, in which more than one domain type are present, can also be detected by measurements of anomalous Hall effect versus out-of-plane magnetic field, because the different domain types have different coercive fields (Extended Data Fig. 1). For convenience in the following, we will adopt pseudo-cubic (pc) notation for $SrRuO_3$ based on the $SrTiO_3$ crystal axes, so that $[100]_{pc}$, $[010]_{pc}$ and $[001]_{pc}$ are parallel to $[\bar{1}10]_o$, $[001]_o$ and $[110]_o$.

In thin films of $SrRuO_3$ the orientation of the canted easy axis is tunable by oxygen octahedral rotation and need not lie exactly along the b axis [51–53]. We therefore performed angular-dependent magnetoresistance measurements to determine the orientation of the magnetic easy axis in our thin films [51, 53]. The device geometry is shown in Fig. 2b, where a longitudinal voltage (V_{XX}) is measured while rotating an external magnetic field ($\vec{B}$) in the plane perpendicular to the applied current. This magnetoresistance measurement was performed on devices oriented at in-plane angles from 0° to 90° at every 15° (Supplementary Information Section 2), to identify both the magnetic canting direction and canting angle. A representative angular-dependent magnetoresistance measurement is shown in Fig. 2c, where the jumps around 115° (295°) in resistance indicate the orientation of the magnetic hard axis (Supplementary Information Section 2). Since the easy-axis angle (θ_C) is 90° from the hard axis, for the 20 nm $SrRuO_3$ film $\theta_C \sim 25°$ away from $[001]_{pc}$ towards $[100]_{pc}$. The canting angle of $SrRuO_3$ of various thicknesses is summarized in Fig. 2d, consistent with previous work [53, 54].

For spin-torque studies, after the $SrRuO_3$ films were grown they were transferred through air to a separate vacuum system for deposition of a 5 nm thick $Ni_{80}Fe_{20}$ (Py) layer by magnetron sputtering on top of the $SrRuO_3$ (Methods). The Py layer has within-plane magnetic anisotropy. For thin $SrRuO_3$ samples (5 nm), where a single domain in the $SrRuO_3$ can be easily achieved (Extended Data Fig. 1b), the spin-torque measurements were performed on the as-grown samples, while the thicker samples (> 5 nm) in which a second type of domain becomes more significant (Extended Data Fig. 1d) were field-cooled to liquid nitrogen temperature with a magnetic field oriented along the $[100]_{pc}$ axis prior to the spin torque measurements. Scans of longitudinal resistance as a function of in-plane magnetic field at 80 K along both the $[100]_{pc}$ and $[010]_{pc}$ are, to a good approximation, symmetric about zero magnetic field (Extended Data Fig. 2), which indicates that any exchange bias between the $SrRuO_3$ and Py is weak.

We measured the direction and strength of current-induced spin torques in the $SrRuO_3$/Py samples using angle-dependent spin torque ferromagnetic resonance (ST-FMR) [5, 15, 25, 55] (Methods). A schematic illustration of our ST-FMR device geometry is shown in Fig. 3a. The device consists of a $SrRuO_3$/Py strip 10 μm $\times$ 40 μm in contact with ground-signal-ground electrodes made from Ti/Pt. Strips with different in-plane orientations relative to the crystal axes were fabricated to study the dependence of spin-orbit torque generation on the angle of applied electric field (or, equivalently, the angle of applied current). On each device with a distinct orientation, we apply a microwave signal with fixed frequency and sweep the external magnetic field $\vec{B}$ at an angle φ to the applied electric-field direction (Fig. 3a), repeating the measurement on the same device for φ from 0° to 170°. An example ST-FMR spectrum at $\varphi = 45°$ is shown in Fig. 3b, where the mixing voltage (V_{mix}) is fit to the sum of symmetric Lorentzian, $V_S = S(\frac{\Delta^2}{(B-B_0)^2+\Delta^2})$, and anti-symmetric

Lorentzian, $V_A = A(\frac{(B-B_0)\Delta}{(B-B_0)^2+\Delta^2})$. Here, S and A are the amplitudes of the symmetric and anti-symmetric components of the mixing voltage, Δ is the linewidth of the resonance peak, and B_0 is the resonant magnetic field. A pronounced difference in the amplitudes of the anti-symmetric component of the mixing voltage at positive and negative fields is observed, indicating the existence of an unconventional torque in the out-of-plane direction. To unambiguously identify the directions of the torques, symmetry analysis is necessary, since the signals generated by different components of torque have different dependencies on the orientations of the external magnetic field. If we define the current flow direction as $\hat{X}$, the out-of-plane direction as $\hat{Z}$, and use polar coordinates to describe the magnetic field with the azimuthal angle φ measured from the $\hat{X}$ direction, then the φ dependence of the mixing voltages from X, Y, Z components of the torques are [15, 25]:

$$V_A = A^X_{FL} \sin 2\varphi \sin\varphi + A^Y_{FL} \sin 2\varphi \cos\varphi + A^Z_{DL} \sin 2\varphi \tag{1}$$

$$V_S = S^X_{DL} \sin 2\varphi \sin\varphi + S^Y_{DL} \sin 2\varphi \cos\varphi + S^Z_{FL} \sin 2\varphi \tag{2}$$

where S^X_{DL}, S^Y_{DL}, A^Z_{DL} are the amplitudes of the mixing voltages contributed by the X, Y, Z components of the damping-like torque; and A^X_{FL}, A^Y_{FL}, S^Z_{FL} are the amplitudes of the mixing voltages from the contributions of the X, Y, Z components of the field-like torque. Two representative angle-dependent ST-FMR results at 110 K are shown in Fig. 3c,d and Fig. 3e,f for a $SrRuO_3$ (5 nm)/Py (5 nm) sample with applied electric fields approximately parallel to the $[010]_{pc}$ and $[100]_{pc}$. For both orientations of $\vec{E}$, fits to both the anti-symmetric and symmetric mixing voltages require additional Z ($\sin 2\varphi$) and X ($\sin 2\varphi \sin\varphi$) components of the torques, in addition to the conventional Y component ($\sin 2\varphi \cos\varphi$). Comparing the ST-FMR results for two perpendicular electric-field directions, the anti-symmetric mixing signals corresponding to the Z component of torque have opposite signs (compare the red lines in Fig. 3c and Fig. 3e). Below we will ascribe this difference to separate contributions from the spin AHE and the PHE spin current.

We have confirmed the presence of the unconventional torque components using a second measurement technique, second harmonic Hall measurements. Angle-dependent second harmonic Hall voltage data for 100 K are shown in Extended Data Fig. 4a and b for the same $SrRuO_3$ (5 nm)/Py (5 nm) sample with applied electric fields approximately parallel to the $[010]_{pc}$ and $[100]_{pc}$. The Z component of the damping-like torques for electric-field along $[010]_{pc}$ and $[100]_{pc}$ have opposite signs, in agreement with the ST-FMR results.

Based on the ST-FMR measurements, the damping-like torque efficiencies can be be calculated as [56]

$$\xi_{DL}^{Y} = S_{DL}^{Y} \frac{eM_S t_{FM}}{\hbar J_e} \frac{4\Delta}{I_{rf} R_{AMR}} \frac{2B_0 + \mu_0 M_{eff}}{\sqrt{B_0(B_0 + \mu_0 M_{eff})}} \tag{3}$$

$$\xi_{DL}^{Z} = A_{DL}^{Z} \frac{eM_S t_{FM}}{\hbar J_e} \frac{4\Delta}{I_{rf} R_{AMR}} \frac{2B_0 + \mu_0 M_{eff}}{B_0 + \mu_0 M_{eff}} \tag{4}$$

where M_s (A/m) is the saturation magnetization for 5 nm of Py, t_{Py} is the thickness of the Py layer, I_{rf} is the amplitude of the microwave current within the full bilayer, J_e is the current density within the $SrRuO_3$, and $\mu_0 M_{eff}$ (T) is the effective field from the magnetic anisotropy. We calibrate I_{rf} by comparing the heating-induced change in resistance due to a microwave current to the heating-induced change of a d.c. current, and then J_e is determined from a parallel circuit model using the measured resistivities of the Py and the $SrRuO_3$ (see Supplementary Information section 3). For the data shown in Fig. 3, $I_{rf} = 2.03$ mA and $J_e = 9.50 \times 10^9$ A/m^2. For the case of $\vec{E}$ along the $[010]_{pc}$, the Y and Z components of the damping-like torque efficiencies estimated with Eq. 3 and Eq. 4 are $\xi_{DL}^{Y} = 0.45 \pm 0.06$ and $\xi_{DL}^{Z} = 0.009 \pm 0.001$. Given that the resistivity (ρ) of $SrRuO_3$ at 110 K is around 231 $\mu\Omega$cm, the spin Hall conductivities estimated using $\sigma_{DL} = (\hbar/2e)\xi_{DL}/\rho$ for the Y and Z components are $\sigma_{DL}^{Y} = (2.0 \pm 0.3) \times 10^5 (\hbar/2e)(\Omega^{-1}\mathrm{m}^{-1})$ and $\sigma_{DL}^{Z} = (3.9 \pm 0.4) \times 10^3 (\hbar/2e)(\Omega^{-1}\mathrm{m}^{-1})$. For $\vec{E}$ along the $[100]_{pc}$, the damping-like torque efficiencies for Y and Z components are estimated to be $\xi_{DL}^{Y} = 0.49 \pm 0.07$ and $\xi_{DL}^{Z} = -0.010 \pm 0.001$; and the corresponding spin Hall conductivities for Y and Z component are $\sigma_{DL}^{Y} = (2.1 \pm 0.3) \times 10^5 (\hbar/2e)(\Omega^{-1}\mathrm{m}^{-1})$ and $\sigma_{DL}^{Z} = (-4.3 \pm 0.4) \times 10^3 (\hbar/2e)(\Omega^{-1}\mathrm{m}^{-1})$.

To investigate the origins of out-of-plane anti-damping torque, the magnetic field angle-dependent ST-FMR measurements were repeated on devices with intermediate ψ angles for the orientation of the applied electric field relative to the $[100]_{pc}$ crystal direction (Fig. 4a). The out-of-plane anti-damping torque efficiency ξ_{DL}^{Z} has the angular dependence shown in Fig. 4b. This behavior of ξ_{DL}^{Z} is in excellent agreement with the predicted dependence for the sum of torques due to the spin AHE ($\propto \sin(\psi)$) and the PHE spin current ($\propto \cos(\psi)$): $\xi_{DL}^{Z} = \xi_{PHE}^{Z} \cos\psi + \xi_{AHE}^{Z} \sin\psi$ for fitting parameters $\xi_{PHE}^{Z} =$ -0.0070 and $\xi_{AHE}^{Z} = 0.0067$ for the 5 nm thick $SrRuO_3$.

In addition to data for the 5 nm device, Fig. 4b also shows the measured out-of-plane anti-damping torque efficiencies ξ_{DL}^{Z} per unit charge density as a function of the electric-field angle ψ for 20 and 30 nm $SrRuO_3$ layer thicknesses. The temperature dependences for the peak out-of-plane anti-damping torque efficiencies for

$SrRuO_3$ of 5 nm, 20 nm and 30 nm are shown in Fig. 4c. We find that ξ^Z_{DL} reaches a peak value at approximately 20 nm, with $\xi^Z_{DL} = 0.020 \pm 0.002$ at 90 K. This peak torque efficiency is greater for 20 nm thick $SrRuO_3$ than for 30 nm despite the fact that the 30 nm thick layer has a comparable canting angle for the magnetization (see Fig. 2d). This difference in torque efficiency could be an indication, e.g., of competing contributions from the larger magnetization canting angle versus a less-perfect domain structure for the 30 nm films (Extended Data Fig. 1), or a contribution from an interfacial torque mechanism and not just a bulk mechanism.

The temperature dependence of ξ^Z_{DL} for a $SrRuO_3$ (5 nm)/Py (5 nm) is shown in Fig. 4d for the electric-field angle $\psi = 120°$, near which the magnitude of ξ^Z_{DL} is maximized. The magnitude of ξ^Z_{DL} decreases with increasing temperature and approaches zero near 135 K, just below the bulk Curie temperature (and remains zero up to room temperature, see Extended Data Fig. 6). (The Curie temperature (T_C) of the $SrRuO_3$ thin films of various thicknesses can be identified from the kink in the resistivity versus temperature curves (Fig. 4e), yielding values of T_C between 130 K and 140 K.) Based on measurements at $\psi = 0°$ and 90°, we can also separate the temperature dependence due to the PHE ($\propto \cos(\psi)$) and spin AHE ($\propto \sin(\psi)$) spin current mechanisms (Fig. 4f). The spin AHE contribution has very little temperature dependence between liquid-nitrogen temperature and 130 K, while the PHE spin current contribution varies strongly in the same temperature range. We speculate that the time-even spin AHE contribution is due primarily to intrinsic spin-orbit coupling within the $SrRuO_3$ bandstructure and is therefore relatively temperature-independent well below the Curie temperature, while the PHE spin current is odd under time reversal and is therefore more likely to depend on extrinsic scattering and other processes which can vary with temperature.

The out-of-plane anti-damping torque efficiency we find from $SrRuO_3$ is less than about half the value needed to directly drive efficient anti-damping switching of nanoscale magnetic samples with PMA, as indicated by modeling [27], and for this reason we have not yet attempted to make prototype nanoscale devices for testing. It is important to distinguish our goal, efficient switching of nanoscale PMA samples, from previous demonstrations of switching in micron-scale samples. Many studies have shown that even very weak out-of-plane torques can assist spin-orbit-torque switching of micron-scale PMA samples, but in all such studies performed to date the critical current is still determined primarily by the conventional in-plane component of spin-orbit torque that acts to shift domain walls, with the out-of-plane component acting only to provide a bit of symmetry breaking required to make the switching “field free”. Studies of spin-orbit switching of micron-scale samples via domain-wall motion are therefore not directly applicable to the development of efficient switching of practical nanoscale PMA devices driven primarily by the out-of-plane anti-damping torque because the switching mechanisms are not the same [14].

In summary, we have demonstrated a strategy for achieving a partly-canted magnetization configuration in a magnetic spin-source layer at zero applied magnetic field, and have shown that this configuration allows for the generation of vertically-flowing spin current with an out-of-plane spin component, which can therefore exert an out-of-plane anti-damping spin-orbit torque on an adjacent magnetic layer. The use of the ferromagnetic moment to provide the symmetry-breaking needed to enable an out-of-plane anti-damping torque circumvents the challenges posed by low-crystalline-symmetry materials and antiferromagnets for switching magnetic memories with perpendicular magnetic anisotropy. Based on the dependence of the out-of-plane torques on the angle of the applied electric field relative to the canted magnetization, the out-of-plane anti-damping torques generated by $SrRuO_3$ can be well-described as due to the sum of a spin AHE and a PHE spin current. The maximum out-of-plane torque efficiency that we measure, $\xi^{Z}_{DL} = 0.020 \pm 0.002$ is still below the threshold needed for spin-orbit-torque MRAM to achieve better energy efficiency than conventional spin-transfer-torque MRAM. (Extended Data Table 1 presents a list of materials systems in which out-of-plane anti-damping torques have been measured quantitatively.) Nonetheless, our study opens the door to explore torque generation by other magnetic materials in which magnetocrystalline anisotropy might be used to stabilize similar partly-canted magnetization configurations [57].

References

1. Bhatti, S., Sbiaa, R., Hirohata, A., Ohno, H., Fukami, S. & Piramanayagam, S. Spintronics based random access memory: a review. *Mater. Today* **20,** 530–548 (2017).
2. Dieny, B. & Chshiev, M. Perpendicular magnetic anisotropy at transition metal/oxide interfaces and applications. *Rev. Mod. Phys.* **89,** 025008 (2017).
3. Mihai Miron, I., Gaudin, G., Auffret, S., Rodmacq, B., Schuhl, A., Pizzini, S., Vogel, J. & Gambardella, P. Current-driven spin torque induced by the Rashba effect in a ferromagnetic metal layer. *Nat. Mater.* **9,** 230–234 (2010).
4. Miron, I. M., Garello, K., Gaudin, G., Zermatten, P.-J., Costache, M. V., Auffret, S., Bandiera, S., Rodmacq, B., Schuhl, A. & Gambardella, P. Perpendicular switching of a single ferromagnetic layer induced by in-plane current injection. *Nature* **476,** 189–193 (2011).
5. Liu, L., Moriyama, T., Ralph, D. & Buhrman, R. Spin-torque ferromagnetic resonance induced by the spin Hall effect. *Phys. Rev. Lett.* **106,** 036601 (2011).
6. Liu, L., Pai, C.-F., Li, Y., Tseng, H., Ralph, D. & Buhrman, R. Spin-torque switching with the giant spin Hall effect of tantalum. *Science* **336,** 555–558 (2012).
7. Mellnik, A. R., Lee, J., Richardella, A., Grab, J. L., Mintun, P. J., Fischer, M. H., Vaezi, A., Manchon, A., Kim, E.-A., Samarth, N., *et al.* Spin-transfer torque generated by a topological insulator. *Nature* **511,** 449–451 (2014).
8. Fan, Y., Upadhyaya, P., Kou, X., Lang, M., Takei, S., Wang, Z., Tang, J., He, L., Chang, L.-T., Montazeri, M., *et al.* Magnetization switching through giant spin-orbit torque in a magnetically doped topological insulator heterostructure. *Nat. Mater.* **13,** 699–704 (2014).
9. Han, J., Richardella, A., Siddiqui, S. A., Finley, J., Samarth, N. & Liu, L. Room-temperature spin-orbit torque switching induced by a topological insulator. *Phys. Rev. Lett.* **119,** 077702 (2017).
10. Wang, Y., Zhu, D., Wu, Y., Yang, Y., Yu, J., Ramaswamy, R., Mishra, R., Shi, S., Elyasi, M., Teo, K.-L., *et al.* Room temperature magnetization switching in topological insulator-ferromagnet heterostructures by spin-orbit torques. *Nat. Commun.* **8,** 1364 (2017).

11. Nan, T., Anderson, T., Gibbons, J., Hwang, K., Campbell, N., Zhou, H., Dong, Y., Kim, G., Shao, D., Paudel, T., *et al.* Anisotropic spin-orbit torque generation in epitaxial $SrIrO_3$ by symmetry design. *PNAS* **116,** 16186–16191 (2019).

12. Huang, X., Sayed, S., Mittelstaedt, J., Susarla, S., Karimeddiny, S., Caretta, L., Zhang, H., Stoica, V. A., Gosavi, T., Mahfouzi, F., *et al.* Novel spin-orbit torque generation at room temperature in an all-oxide epitaxial $La_{0.7}Sr_{0.3}MnO_3/SrIrO_3$ system. *Adv. Mater.* **33,** 2008269 (2021).

13. Garello, K., Miron, I. M., Avci, C. O., Freimuth, F., Mokrousov, Y., Blügel, S., Auffret, S., Boulle, O., Gaudin, G. & Gambardella, P. Symmetry and magnitude of spin–orbit torques in ferromagnetic heterostructures. *Nat. Nanotechnol.* **8,** 587–593 (2013).

14. Zhang, C., Fukami, S., Sato, H., Matsukura, F. & Ohno, H. Spin-orbit torque induced magnetization switching in nano-scale Ta/CoFeB/MgO. *Appl. Phys. Lett.* **107,** 012401 (2015).

15. MacNeill, D., Stiehl, G., Guimaraes, M., Buhrman, R., Park, J. & Ralph, D. Control of spin-orbit torques through crystal symmetry in WTe_2/ferromagnet bilayers. *Nat. Phys.* **13,** 300–305 (2017).

16. Liu, L., Zhou, C., Shu, X., Li, C., Zhao, T., Lin, W., Deng, J., Xie, Q., Chen, S., Zhou, J., *et al.* Symmetry-dependent field-free switching of perpendicular magnetization. *Nat. Nanotechnol.* **16,** 277–282 (2021).

17. DC, M., Shao, D.-F., Hou, V. D.-H., Vailionis, A., Quarterman, P., Habiboglu, A., Venuti, M., Xue, F., Huang, Y.-L., Lee, C.-M., *et al.* Observation of anti-damping spin-orbit torques generated by in-plane and out-of-plane spin polarizations in $MnPd_3$. *Nat. Mater.* **22,** 591–598 (2023).

18. Liu, Y., Shi, G., Kumar, D., Kim, T., Shi, S., Yang, D., Zhang, J., Zhang, C., Wang, F., Yang, S., *et al.* Field-free switching of perpendicular magnetization at room temperature using out-of-plane spins from $TaIrTe_4$. *Nat. Electron.* **6,** 732–738 (2023).

19. Patton, M., Gurung, G., Shao, D.-F., Noh, G., Mittelstaedt, J. A., Mazur, M., Kim, J.-W., Ryan, P. J., Tsymbal, E. Y., Choi, S.-Y., *et al.* Symmetry control of unconventional spin-orbit torques in IrO_2. *Adv. Mater.* **35,** 2301608 (2023).

20. Taniguchi, T., Grollier, J. & Stiles, M. D. Spin-transfer torques generated by the anomalous Hall effect and anisotropic magnetoresistance. *Phys. Rev. Appl.* **3,** 044001 (2015).

21. Železnỳ, J., Zhang, Y., Felser, C. & Yan, B. Spin-polarized current in non-collinear antiferromagnets. *Phys. Rev. Lett.* **119,** 187204 (2017).

22. Iihama, S., Taniguchi, T., Yakushiji, K., Fukushima, A., Shiota, Y., Tsunegi, S., Hiramatsu, R., Yuasa, S., Suzuki, Y. & Kubota, H. Spin-transfer torque induced by the spin anomalous Hall effect. *Nat. Electron.* **1,** 120–123 (2018).

23. Nan, T., Quintela, C. X., Irwin, J., Gurung, G., Shao, D.-F., Gibbons, J., Campbell, N., Song, K., Choi, S.-Y., Guo, L., *et al.* Controlling spin current polarization through non-collinear antiferromagnetism. *Nat. Commun.* **11,** 4671 (2020).

24. Chen, X., Shi, S., Shi, G., Fan, X., Song, C., Zhou, X., Bai, H., Liao, L., Zhou, Y., Zhang, H., *et al.* Observation of the antiferromagnetic spin Hall effect. *Nat. Mater.* **20,** 800–804 (2021).

25. Bose, A., Schreiber, N. J., Jain, R., Shao, D.-F., Nair, H. P., Sun, J., Zhang, X. S., Muller, D. A., Tsymbal, E. Y., Schlom, D. G., *et al.* Tilted spin current generated by the collinear antiferromagnet ruthenium dioxide. *Nat. Electron.* **5,** 267–274 (2022).

26. Chen, H., Jiang, D., Zhang, Y., Qiu, X., Liang, Y., Zhang, Q., Zhu, F., Ohkochi, T., Chen, M., Wang, Y., *et al.* Pure spin current polarizer enabled by antiferromagnetic insulator. *Nat. Commun.* **16,** 6257 (2025).

27. Liao, Y.-C., Kumar, P., Li, X., Zhang, D., Wang, J.-P., Wang, S. X., Ralph, D. C., Naeemi, A., *et al.* Spin-orbit-torque material exploration for maximum array-level read/write performance. *2020 IEEE International Electron Devices Meeting (IEDM)* 13–6. 2020

28. Zhang, Y., Xu, H., Jia, K., Lan, G., Huang, Z., He, B., He, C., Shao, Q., Wang, Y., Zhao, M., Ma, T., Dong, J., Guo, C., Cheng, C., Feng, J., Wan, C., Wei, H., Shi, Y., Zhang, G., Han, X. & Yu, G. Room temperature field-free switching of perpendicular magnetization through spin-orbit torque originating from low-symmetry type II Weyl semimetal. *Sci. Adv.* **9,** eadg9819 (2023).

29. Bainsla, L., Zhao, B., Behera, N., Hoque, A. M., Sjöström, L., Martinelli, A., Abdel-Hafiez, M., Åkerman, J. & Dash, S. P. Large out-of-plane spin-orbit torque in topological Weyl semimetal $TaIrTe_4$. *Nat. Commun.* **15,** 4649 (2024).

30. Amin, V. P., Li, J., Stiles, M. D. & Haney, P. M. Intrinsic spin currents in ferromagnets. *Phys. Rev. B* **99,** 220405 (2019).

31. Davidson, A., Amin, V. P., Aljuaid, W. S., Haney, P. M. & Fan, X. Perspectives of electrically generated spin currents in ferromagnetic materials. *Phys. Lett. A* **384,** 126228 (2020).

32. Seki, T., Iihama, S., Taniguchi, T. & Takanashi, K. Large spin anomalous Hall effect in $L1_0$-FePt: Symmetry and magnetization switching. *Phys. Rev. B* **100,** 144427 (2019).

33. Montoya, E. A., Pei, X. & Krivorotov, I. N. Anomalous Hall spin current drives self-generated spin–orbit torque in a ferromagnet. *Nat. Nanotechnol.* **20,** 353–359 (2025).

34. Safranski, C., Montoya, E. A. & Krivorotov, I. N. Spin-orbit torque driven by a planar Hall current. *Nat. Nanotechnol.* **14,** 27–30 (2019).

35. Safranski, C., Sun, J. Z., Xu, J.-W. & Kent, A. D. Planar Hall driven torque in a ferromagnet/nonmagnet/ferromagnet system. *Phys. Rev. Lett.* **124,** 197204 (2020).

36. Saidaoui, H. B. M. & Manchon, A. Spin-swapping transport and torques in ultrathin magnetic bilayers. *Phys. Rev. Lett.* **117,** 036601 (2016).

37. Humphries, A. M., Wang, T., Edwards, E. R., Allen, S. R., Shaw, J. M., Nembach, H. T., Xiao, J. Q., Silva, T. J. & Fan, X. Observation of spin-orbit effects with spin rotation symmetry. *Nat. commun.* **8,** 911 (2017).

38. Baek, S.-h. C., Amin, V. P., Oh, Y.-W., Go, G., Lee, S.-J., Lee, G.-H., Kim, K.-J., Stiles, M. D., Park, B.-G. & Lee, K.-J. Spin currents and spin-orbit torques in ferromagnetic trilayers. *Nat. Mater.* **17,** 509–513 (2018).

39. Amin, V. P., Zemen, J. & Stiles, M. D. Interface-generated spin currents. *Phys. Rev. Lett.* **121,** 136805 (2018).

40. Yang, Q., Han, D., Zhao, S., Kang, J., Wang, F., Lee, S.-C., Lei, J., Lee, K.-J., Park, B.-G. & Yang, H. Field-free spin-orbit torque switching in ferromagnetic trilayers at sub-ns timescales. *Nat. Commun.* **15,** 1814 (2024).

41. Ou, Y., Wang, Z., Chang, C. S., Nair, H. P., Paik, H., Reynolds, N., Ralph, D. C., Muller, D. A., Schlom, D. G. & Buhrman, R. A. Exceptionally High, Strongly Temperature Dependent, Spin Hall Conductivity of $SrRuO_3$. *Nano Lett.* **19,** 3663–3670 (2019).

42. Wei, J., Zhong, H., Liu, J., Wang, X., Meng, F., Xu, H., Liu, Y., Luo, X., Zhang, Q., Guang, Y., *et al.* Enhancement of spin-orbit torque by strain engineering in $SrRuO_3$ films. *Adv. Funct. Mater.* **31,** 2100380 (2021).

43. Zhou, J., Shu, X., Lin, W., Shao, D. F., Chen, S., Liu, L., Yang, P., Tsymbal, E. Y. & Chen, J. Modulation of spin-orbit torque from $SrRuO_3$ by epitaxial-strain-induced octahedral rotation. *Adv. Mater.* **33,** 2007114 (2021).

44. Longo, J., Raccah, P. & Goodenough, J. Magnetic properties of $SrRuO_3$ and $CaRuO_3$. *J. Appl. Phys.* **39,** 1327–1328 (1968).

45. Schreiber, N. J., Miao, L., Nair, H. P., Ruf, J. P., Bhatt, L., Birkholzer, Y. A., Kotsonis, G. N., Kourkoutis, L. F., Shen, K. M. & Schlom, D. G. Enhanced T_C in $SrRuO_3/DyScO_3$ (110) thin films with high residual resistivity ratio. *APL Mater.* **11** (2023).

46. Jones, C., Battle, P., Lightfoot, P. & Harrison, W. The structure of $SrRuO_3$ by time-of-flight neutron powder diffraction. *Acta Crystallogr. Sect. C: Cryst. Struct. Commun.* **45,** 365–367 (1989).

47. Gan, Q., Rao, R., Eom, C., Wu, L. & Tsui, F. Lattice distortion and uniaxial magnetic anisotropy in single domain epitaxial (110) films of $SrRuO_3$. *J. Appl. Phys.* **85,** 5297–5299 (1999).

48. Koster, G., Klein, L., Siemons, W., Rijnders, G., Dodge, J. S., Eom, C.-B., Blank, D. H. & Beasley, M. R. Structure, physical properties, and applications of $SrRuO_3$ thin films. *Rev. Mod. Phys.* **84,** 253 (2012).

49. Gan, Q., Rao, R. & Eom, C. Control of the growth and domain structure of epitaxial $SrRuO_3$ thin films by vicinal (001) $SrTiO_3$ substrates. *Appl. Phys. Lett.* **70,** 1962–1964 (1997).

50. Jiang, J., Tian, W., Pan, X., Gan, Q. & Eom, C. Domain structure of epitaxial $SrRuO_3$ thin films on miscut (001) $SrTiO_3$ substrates. *Appl. Phys. Lett.* **72,** 2963–2965 (1998).

51. Lu, W., Yang, P., Song, W. D., Chow, G. M. & Chen, J. S. Control of oxygen octahedral rotations and physical properties in $SrRuO_3$ films. *Phys. Rev. B* **88,** 214115 (2013).

52. Lu, W., Song, W., Yang, P., Ding, J., Chow, G. M. & Chen, J. Strain engineering of octahedral rotations and physical properties of $SrRuO_3$ films. *Sci. Rep.* **5,** 10245 (2015).

53. Liu, L., Qin, Q., Lin, W., Li, C., Xie, Q., He, S., Shu, X., Zhou, C., Lim, Z., Yu, J., *et al.* Current-induced magnetization switching in all-oxide heterostructures. *Nat. Nanotechnol.* **14,** 939–944 (2019).

54. Yoo, Y., Chmaissem, O., Kolesnik, S., Ullah, A., Lurio, L., Brown, D., Brady, J., Dabrowski, B., Kimball, C., Haji-Sheikh, M., *et al.* Diverse effects of two-dimensional and step flow growth mode induced microstructures on the magnetic anisotropies of $SrRuO_3$ thin films. *Appl. Phys. Lett.* **89** (2006).

55. Fang, D., Kurebayashi, H., Wunderlich, J., Vỳbornỳ, K., Zârbo, L. P., Campion, R., Casiraghi, A., Gallagher, B., Jungwirth, T. & Ferguson, A. Spin-orbit-driven ferromagnetic resonance. *Nat. Nanotechnol.* **6,** 413–417 (2011).

56. Karimeddiny, S., Mittelstaedt, J. A., Buhrman, R. A. & Ralph, D. C. Transverse and longitudinal spin-torque ferromagnetic resonance for improved measurement of spin-orbit torque. *Phys. Rev. Appl.* **14,** 024024 (2020).

57. Belashchenko, K. Exchange-driven spin Hall effect in anisotropic ferromagnets. *Phys. Rev. B* **109,** 054409 (2024).

58. Stiehl, G. M., Li, R., Gupta, V., Baggari, I. E., Jiang, S., Xie, H., Kourkoutis, L. F., Mak, K. F., Shan, J., Buhrman, R. A., *et al.* Layer-dependent spin-orbit torques generated by the centrosymmetric transition metal dichalcogenide β-$MoTe_2$. *Phys. Rev. B* **100,** 184402 (2019).

59. Wang, F., Shi, G., Kim, K.-W., Park, H.-J., Jang, J. G., Tan, H. R., Lin, M., Liu, Y., Kim, T., Yang, D., *et al.* Field-free switching of perpendicular magnetization by two-dimensional $PtTe_2/WTe_2$ van der Waals heterostructures with high spin Hall conductivity. *Nat. Mater.* **23,** 768–774 (2024).

Methods

Sample preparation

$SrRuO_3$ thin films were grown with pulsed laser deposition (PLD). The thin films were grown on slightly miscut (001)-oriented $SrTiO_3$ substrates at 700 °C, 100 mTorr oxygen partial pressure, and a laser energy of 1.5 J/cm^2 at 2 Hz. After growth, the samples were cooled down at 5 °C/min to room temperature at an atmospheric oxygen pressure. The detection magnet layer (Py) was deposited in an AJA magnetron sputterer system with a base pressure of 2×10^{-8} Torr. A 1.5 nm Ta capping layer was then deposited on the Py to inhibit oxidation.

Device fabrication

ST-FMR and Hall devices with various ψ angles to the crystal axis were patterned using a Heidelberg laser direct writer. The $SrRuO_3$ layer was etched with $NaIO_4$ solution (0.1 mol/L) and other layers were etched by ion milling. Contacts made from Pt (100 nm)/Ti (5 nm) were sputtered in an AJA chamber and then lifted off. For ST-FMR devices, strips with dimension 10 μm $\times$ 40 μm were in contact with ground-signal-ground electrodes. For Hall devices, the dimensions of the Hall bar were 20 μm $\times$ 50 μm.

Magnetoresistance measurement

Hall devices with various in-plane orientations (ψ) were patterned on $SrRuO_3$/Py samples. A direct current of 100 μA was applied with Keithley 2400 d.c. current source meter in the current channel and a longitudinal voltage was measured with Keithley 2181A nanovoltemeter. For the magnetic-field-angle dependent magnetoresistance measurements, an external magnetic field was rotated in a plane perpendicular to the applied current. The measurements were repeated on devices with in-plane orientation ψ from 0° to 90° at every 15° to identify both the magnet canting direction and canting angle. To investigate the exchange coupling between $SrRuO_3$ and Py, the external magnetic field was swept in the plane from positive to negative along the current direction, while recording the longitudinal voltage. The measurement was repeated on devices oriented along both the $[100]_{pc}$ and $[010]_{pc}$ directions.

ST-FMR measurement

ST-FMR devices with ground-signal-ground (GSG) contacts were fabricated from the $SrRuO_3$/Py bilayers. A microwave current at a fixed frequency (5 GHz - 5.5 GHz) and power was applied. A dc mixing voltage was measured with a DSP lockin amplifier while sweeping the external magnetic field from positive to negative at a fixed angle (φ) to the applied current. The same ST-FMR measurement was repeated at magnetic field angles φ from 0° to 170° at every 10°. This magnetic-field-angle-dependent ST-FMR measurement was performed on devices with applied-current angles ψ (in the film plane relative to the $[100]_{pc}$ direction) from 0° to 165° in 15° increments. The temperature-dependent ST-FMR measurements were carried out in a home-built cryostat cooled by liquid nitrogen.

Acknowledgements

X.H. was supported by the US Department of Energy (DOE), Office of Basic Energy Sciences (BES) under award number DE-SC0017671. D.P., D.G.S., and D.C.R. acknowledge support from SUPREME, one of seven centers in JUMP 2.0, a Semiconductor Research Corporation program sponsored by DARPA. Z.T. acknowledges that this work is supported by the Air Force Office of Scientific Research under award number FA9550-24-1-0266. Any opinions, findings, and conclusions or recommendations expressed in this material are those of the author(s) and do not necessarily reflect the views of the United States Air Force. L.W.M. acknowledges support from the the National Science Foundation under Grant DMR-2329111. T.M.J.C. and M.O. were supported in part by the US National Science Foundation (NSF) under DMR-2104268. C.B.E. acknowledges support from Vannevar Bush Faculty Fellowship (ONR N00014-20-1-2844), and the Gordon and Betty Moore Foundation's EPiQS Initiative, Grant No. GBMF9065. Thin Film Synthesis at the University of

Wisconsin–Madison was supported by the U.S. Department of Energy, Office of Science, Office of Basic Energy Sciences, under Award No. DE-FG02-06ER46327. The devices were fabricated using the shared facilities of the Cornell NanoScale Facility, a member of the National Nanotechnology Coordinated Infrastructure (supported by the NSF via grant NNCI-2025233) and the facilities of the Cornell Center for Materials research.

Author contributions

X.H. and D.C.R. conceived and designed the research. Z.T., Y.L., K.L., and C.W. carried out the oxide thin film growth. X.H. and M.O. performed the magnetron sputtering. X.H. and T.M.J.C. carried out the low temperature ST-FMR measurements with help from D.A.P. X.H. did the device fabrication with help from D.A.P. X.H. and D.A.P. performed the angle-dependent magnetoresistance measurements. T.M.J.C. simulated the angular-dependent magnetoresistance. H.Z. and D.F.S. performed the phenomenological symmetry analysis. Y.L., D.Y., C.B.E., D.G.S., and L.W.M. gave suggestions on the experiments. All authors discussed the results and assisted in the preparation of the manuscript.

Competing interests

The authors declare no competing interests

Additional information

Correspondence and requests for materials should be addressed to X.H. and D.C.R.

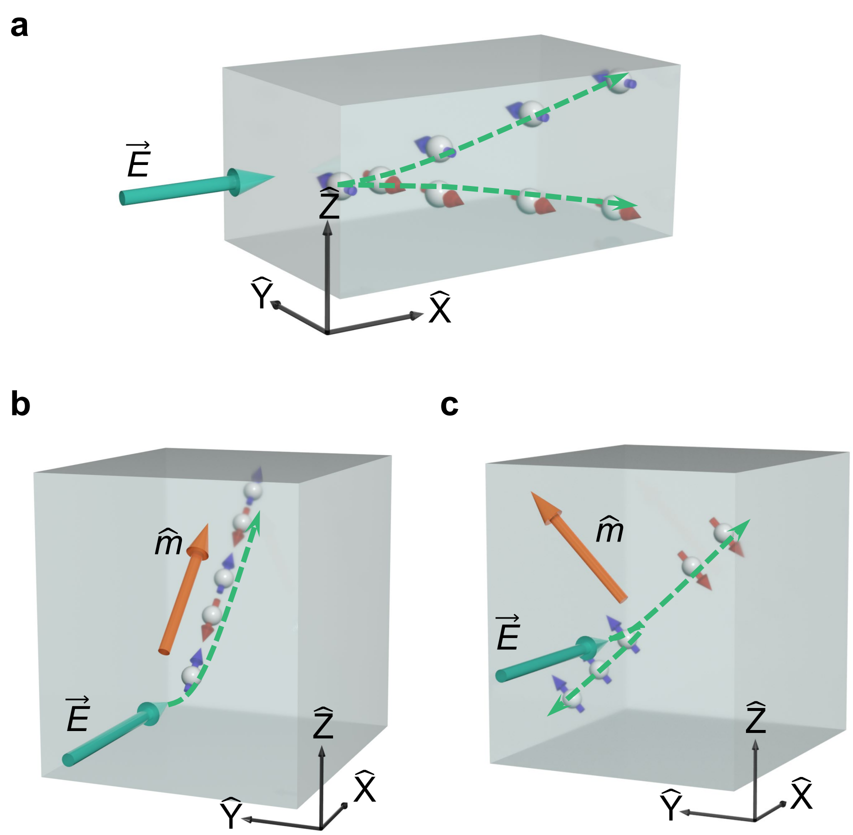

Figure 1: Tilted spin currents produced by a canted magnetization. a, Illustration of the spin current allowed by symmetry for a non-magnetic material with high crystal symmetry, for which a spin current flowing in the $\hat{Z}$ direction must have spin polarization oriented in the $\pm\hat{Y}$ direction. **b,** Illustration of a tilted spin current originating from the planar Hall effect in a ferromagnet, relevant for the case in which an electric field ($\vec{E}$) is applied along the $\hat{X}$ direction and the magnetic moment is canted away from the $\hat{Z}$ direction into the $\hat{X}$ direction. **c,** Illustration of a tilted spin current originating from the spin anomalous Hall effect in a ferromagnet, relevant for the case in which the magnetic moment is canted away from the $\hat{Z}$ direction into the $\hat{Y}$ direction.

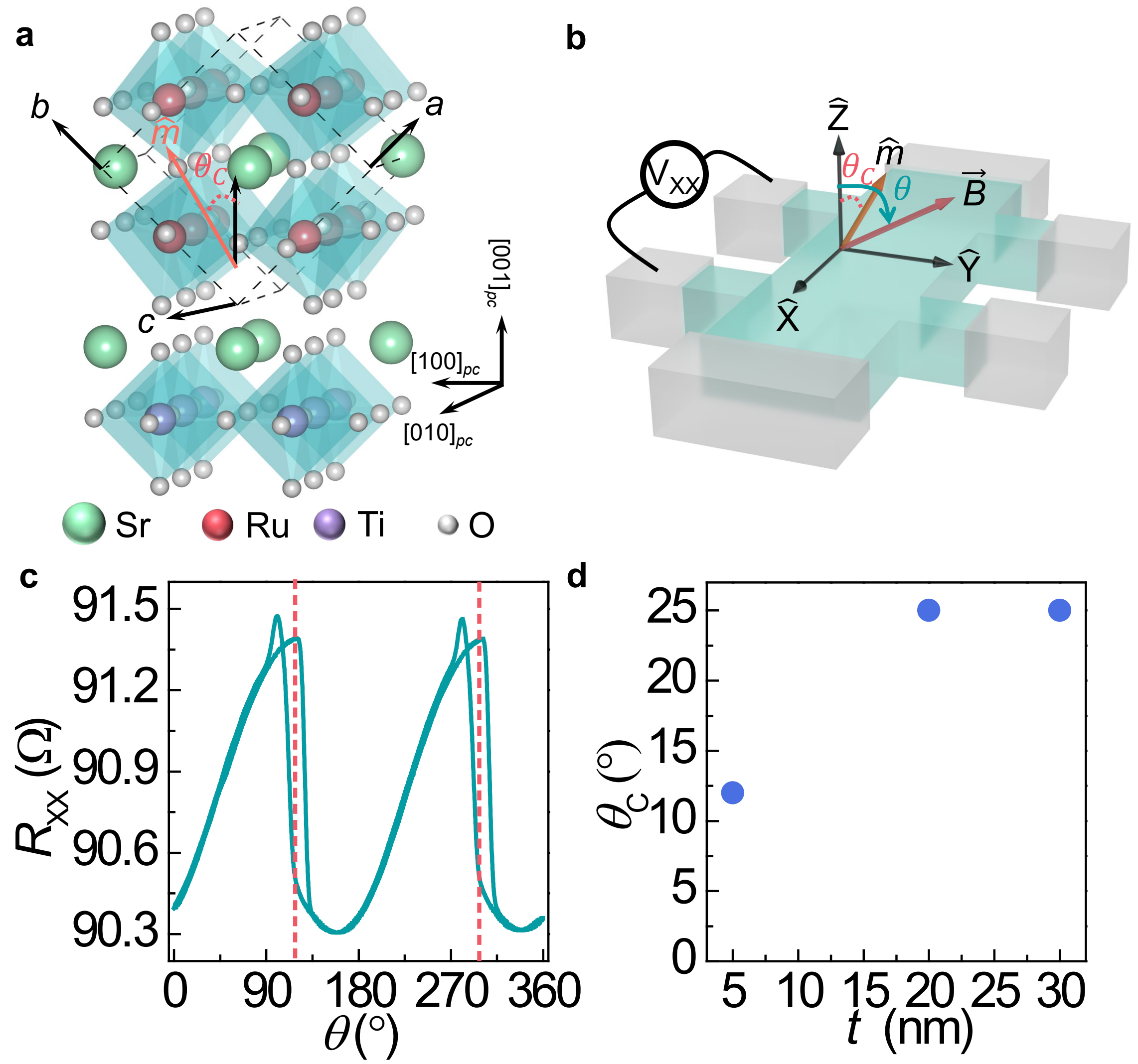

Figure 2: Magnetic anisotropy of $SrRuO_3$ thin films. a, A side view showing the epitaxial relationship of $SrRuO_3$ grown on an (001)-oriented $SrTiO_3$ substrate, where the $[010]_{pc}$ axis points out of the page. a, b, and c are the orthorhombic unit cell axes of $SrRuO_3$. In thin films, the direction of the magnetic easy axis (θ_C) can differ from the b axis. **b,** Device geometry for the angular-dependent magnetoresistance measurements. A longitudinal voltage (V_{XX}) is recorded while rotating the external magnetic field ($\vec{B}$) in a plane perpendicular to the applied current. θ is the external magnetic field angle from the surface normal ($[001]_{pc}$). **c,** An example angular dependent magnetoresistance measurement at 10 K, where longitudinal resistance (R_{XX}) is plotted as a function of magnetic field angle θ for a sample $SrRuO_3$(20 nm)/Py (5 nm). A d.c. current of 100 μA is applied along the $[010]_{pc}$ orientation and a magnetic field 6 T is rotated in the $(010)_{pc}$ plane. **d,** Summary of the easy-axis tilt angle (θ_C) for $SrRuO_3$ films of various thicknesses (t) at 10 K.

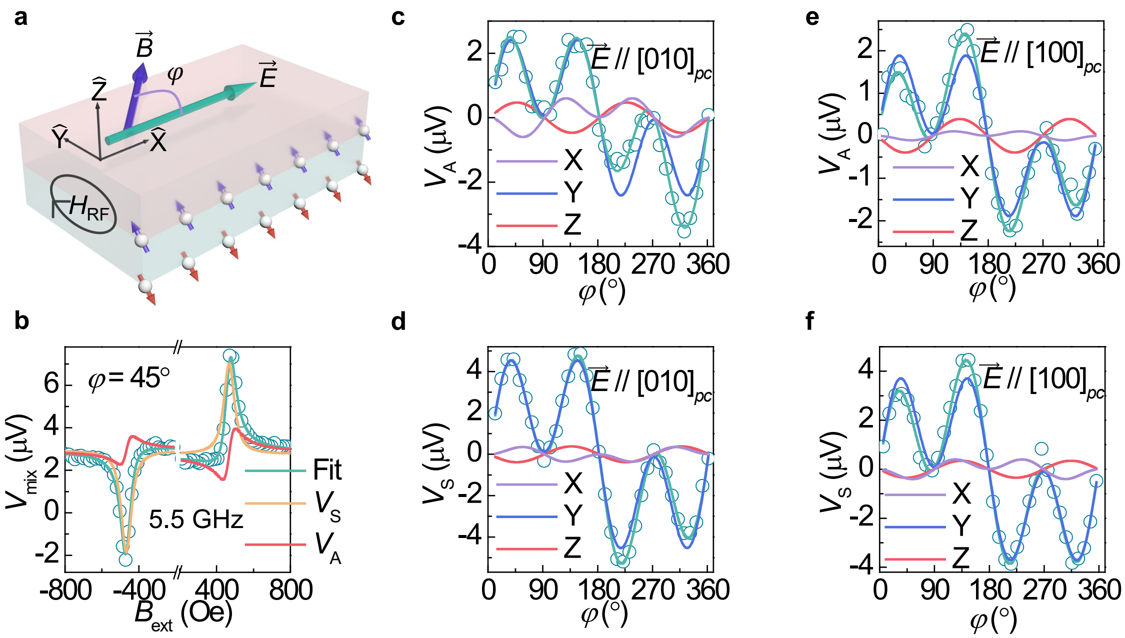

Figure 3: Spin torques characterized by spin-torque ferromagnetic resonance. a, A schematic of a $SrRuO_3$ (5 nm)/Py (5 nm) bilayer used in the ST-FMR measurements. Red layer: Py; Teal layer: $SrRuO_3$; H_{RF}: Oersted field produced by the applied microwave current; $\vec{B}$: external magnetic field; $\vec{E}$: electric field; φ: angle between external magnetic field and microwave current. **b,** Example ST-FMR spectrum, with the d.c. mixing voltage (V_{mix}) plotted as a function of external magnetic field (B). In this example, the ST-FMR measurement is done at 110 K with E along $[010]_{pc}$ and $\varphi = 45°$. The red and orange curves represent the anti-symmetric (V_A) and symmetric (V_S) components of the mixing voltage respectively. **c,** Anti-symmetric mixing voltage as a function of magnetic field angle. X (purple), Y (blue), Z (red) components of the anti-symmetric mixing voltages are determined as the fit components proportional to $\sin(2\varphi)\sin\varphi$, $\sin(2\varphi)\cos\varphi$ and $\sin(2\varphi)$ respectively. **d,** Symmetric mixing voltage as a function of magnetic field angle. X (purple), Y (blue) and Z (red) components of the symmetric mixing voltages are determined as the fit components proportional to $\sin(2\varphi)\cos\varphi$, $\sin(2\varphi)\cos\varphi$ and $\sin(2\varphi)$ respectively. The electric field is applied approximately along the $[010]_{pc}$ crystallographic axis in the plane for **c** and **d**. **e, f** Anti-symmetric and symmetric mixing voltages as a function of magnetic field angle for an electric field applied approximately along the $[100]_{pc}$ crystallographic axis.

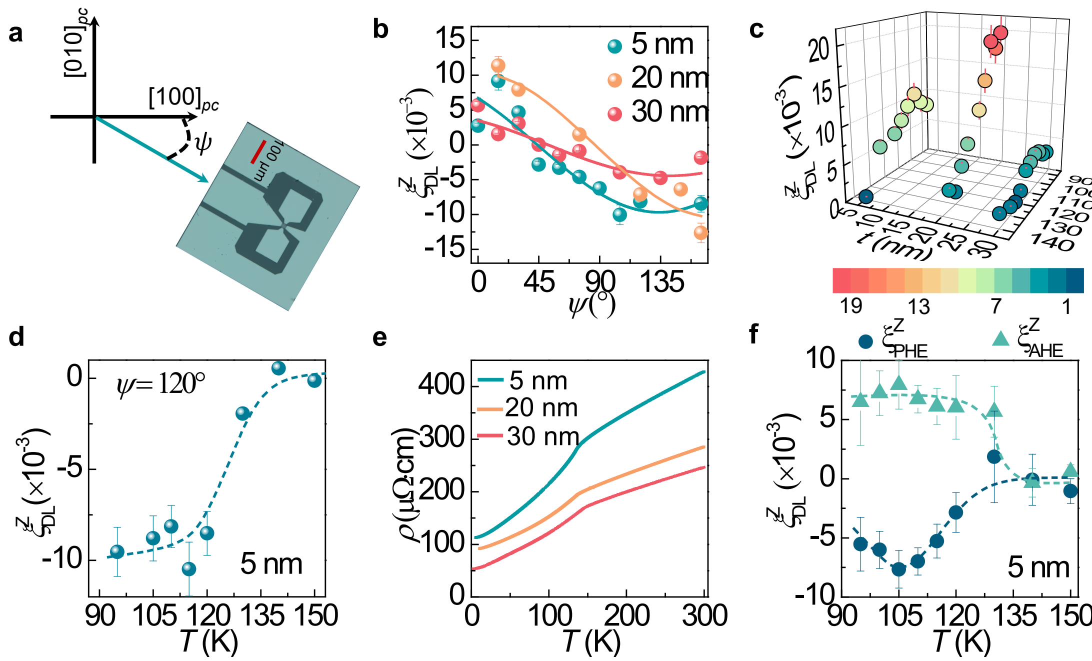

Figure 4: Dependence of out-of-plane anti-damping torque on the orientation of the applied electric field and temperature. a, A schematic of the ST-FMR measurement geometry, for $\vec{E}$ is oriented at a ψ angle to $[100]_{pc}$. **b,** Out-of-plane anti-damping torque efficiency as a function of ψ for a $SrRuO_3$ (5 nm)/Py (5 nm) sample (110 K), a $SrRuO_3$ (20 nm)/Py (5 nm) sample (110 K), and a $SrRuO_3$ (30 nm)/Py (5 nm) sample (105 K). The solid curves represent fits to the data as a linear superposition of $\sin\psi$ and $\cos\psi$, used to determine the AHE and PHE contributions as in panel **f** below. **c,** Temperature dependent out-of-plane damping-like torque efficiency for $SrRuO_3$ of 5 nm, 20 nm and 30 nm. **d,** Representative temperature dependent out-of-plane anti-damping torque efficiency at $\psi = 120°$ for the $SrRuO_3$ (5 nm)/Py (5 nm) sample. The dashed line is a guide to the eye. **e,** Resistivity as a function of temperature for $SrRuO_3$ of various thicknesses. **f,** The PHE (ξ^Z_{PHE}) and AHE (ξ^Z_{AHE}) components of the out-of-plane anti-damping torque efficiencies as a function of temperature for 5 nm $SrRuO_3$. The dashed lines are a guide to the eye. Error bars in **b, c, d** are dominated by the uncertainties of film thicknesses, and error bars in **f** represent fitting uncertainties.

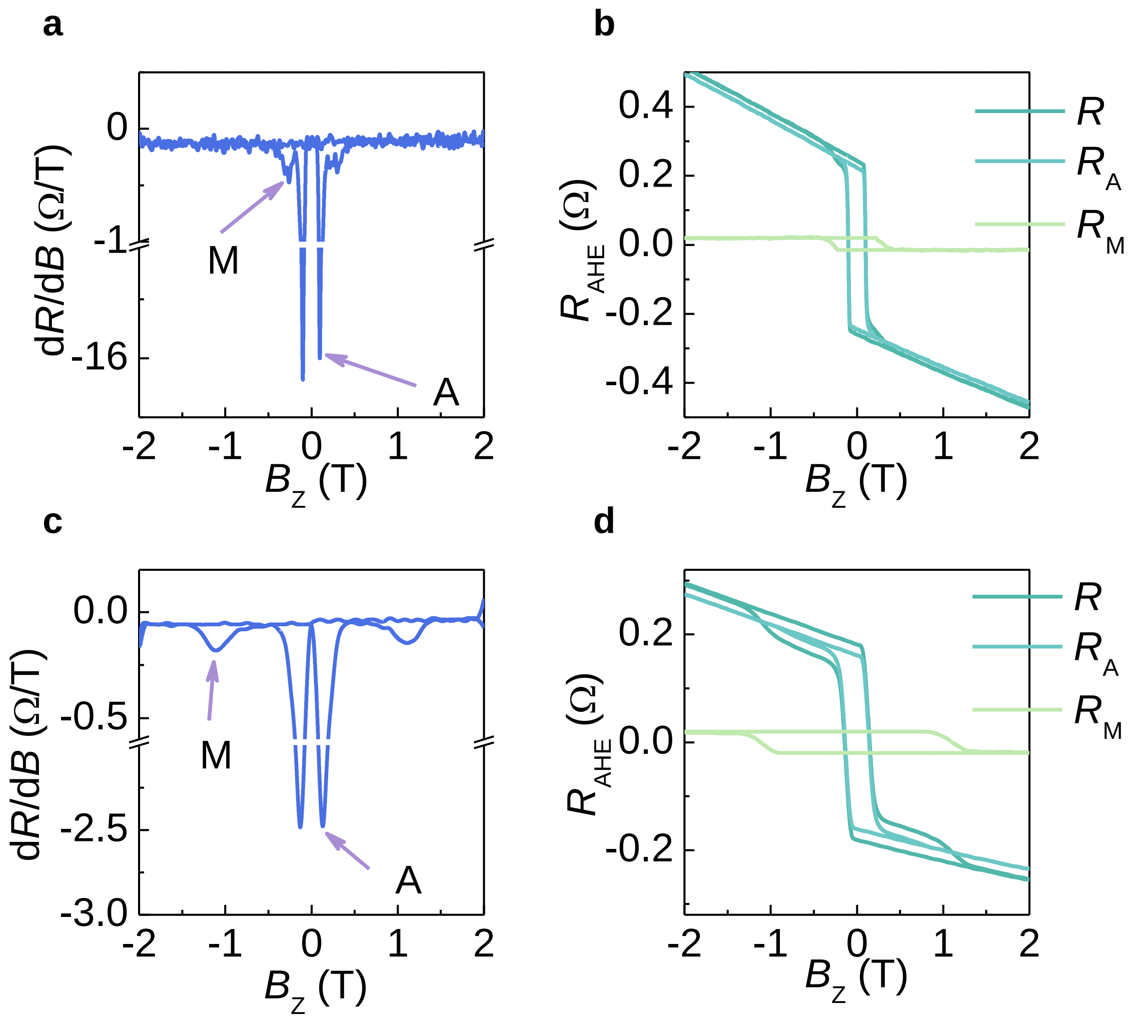

Extended Data Fig. 1. Domain structure characterized using anomalous Hall effect measurements. a, The first derivative of anomalous Hall resistance as a function of external magnetic field for a single-layer 5 nm $SrRuO_3$ thin film at 110 K. 'A' denotes the dominant domain and 'M' denotes minor domains present in the sample. **b,** Anomalous Hall resistance for the same single-layer 5 nm $SrRuO_3$ thin film at 110 K. R_A and R_M are the contributions from the 'A' domain and the minor domain to the anomalous Hall resistance. **c,** The first derivative of anomalous Hall resistance as a function of external magnetic field for a 10 nm $SrRuO_3$ thin film at 110 K. **d,** Anomalous Hall resistance for the same 10 nm $SrRuO_3$ film at 110 K.

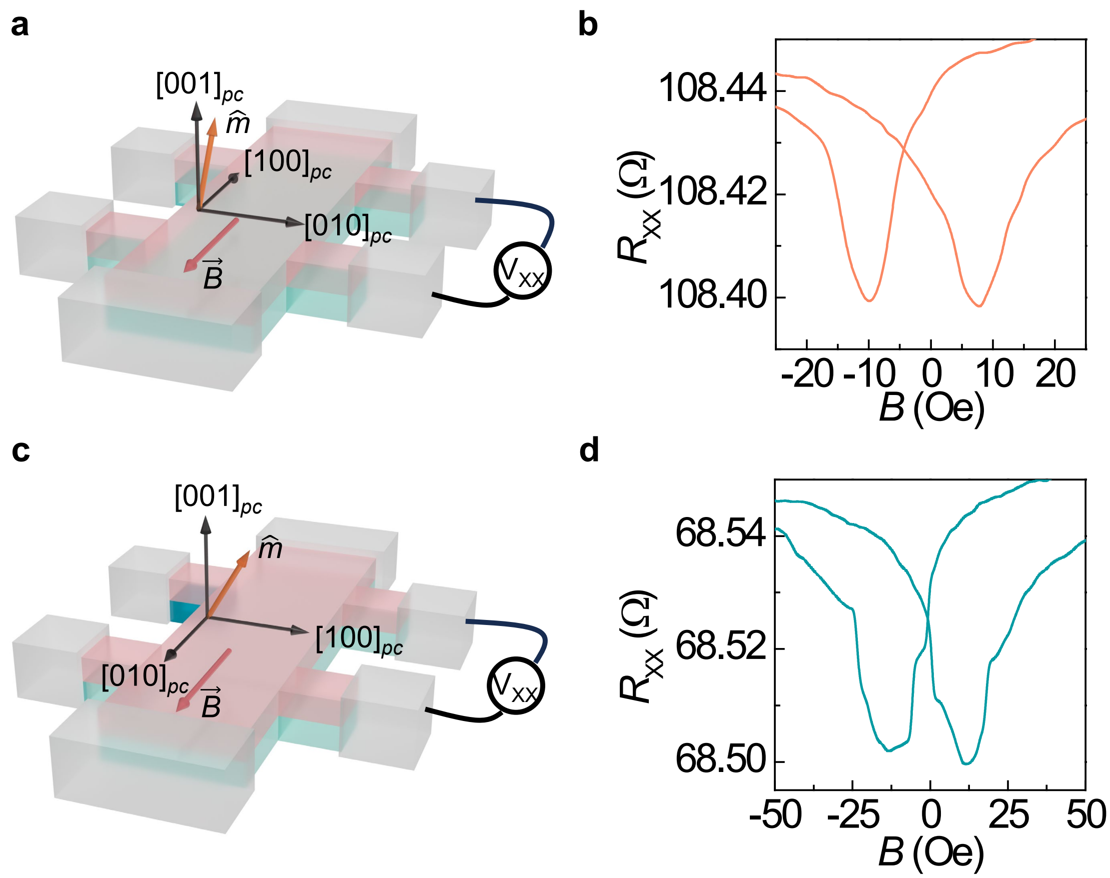

Extended Data Fig. 2. A check for exchange coupling between $SrRuO_3$ (10 nm) and Py (5 nm). a, Schematic illustration of the measurement geometry to test for exchange coupling along the $[100]_{pc}$ direction. Longitudinal voltage (V_{XX}) is measured while an external magnetic field is swept along the $[100]_{pc}$ direction. **b,** Measured longitudinal resistance as a function of external magnetic field at 80 K for the geometry in panel **a**. Two dips are observed, at 8 Oe and -10 Oe, indicating the absence of any significant exchange bias along the $[100]_{pc}$ direction. **c,** Measurement geometry to test for exchange coupling along the $[010]_{pc}$ direction. **d,** Measured longitudinal resistance as a function of external magnetic field at 80 K for the geometry in panel **c**. Two dips are observed symmetrically located at ± 13 Oe, indicating the absence of exchange bias along $[010]_{pc}$ direction.

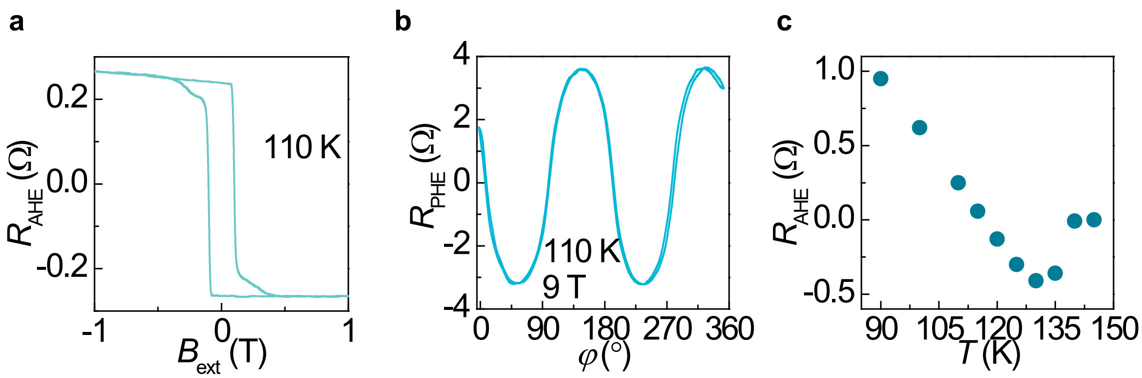

Extended Data Fig. 3. Anomalous Hall and planar Hall effects. a, Anomalous Hall resistance for a 5 nm $SrRuO_3$ film at 110 K. **b,** Planar Hall effect for the same 5 nm $SrRuO_3$ sample at 110 K. An external magnetic field of 9 T is applied. **c,** Anomalous Hall resistance as a function of temperature for the 5 nm $SrRuO_3$ film.

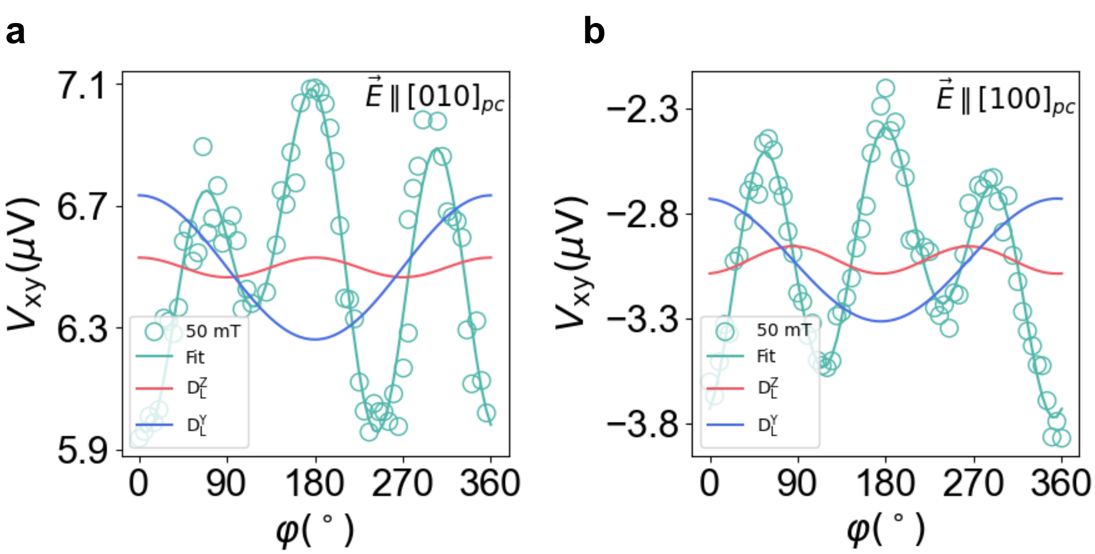

Extended Data Fig. 4. Second harmonic Hall voltage measurements for the sample $SrRuO_3$ (5 nm)/Py (5 nm) at 100 K. a, b, Second harmonic Hall voltages (V_{xy}) as a function of the in-plane orientation (φ) of a magnetic field of 50 mT for electric field ($\vec{E}$) along $[010]_{pc}$ and $[100]_{pc}$ respectively.

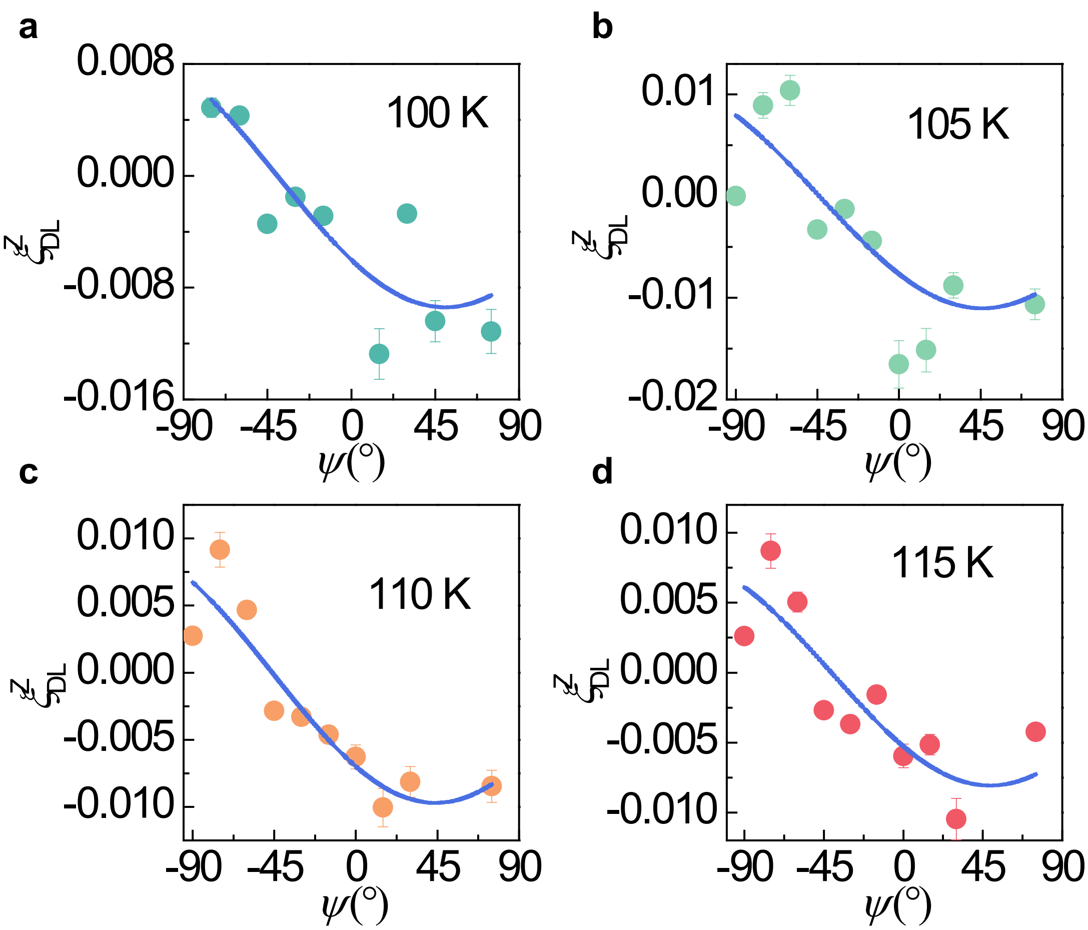

Extended Data Fig. 5. Measured out-of-plane anti-damping torque efficiencies at various temperatures. a, b, c, d, Out-of-plane damping-like torque efficiency as a function of the angle ψ of the applied electric field at 100 K, 105 K, 110 K and 115 K, respectively. The curves in blue are fits to the data of the form $\xi^Z_{DL} = \xi^Z_{AHE} \sin\psi + \xi^Z_{PHE} \cos\psi$. Error bars are calculated based on the uncertainties of film thicknesses.

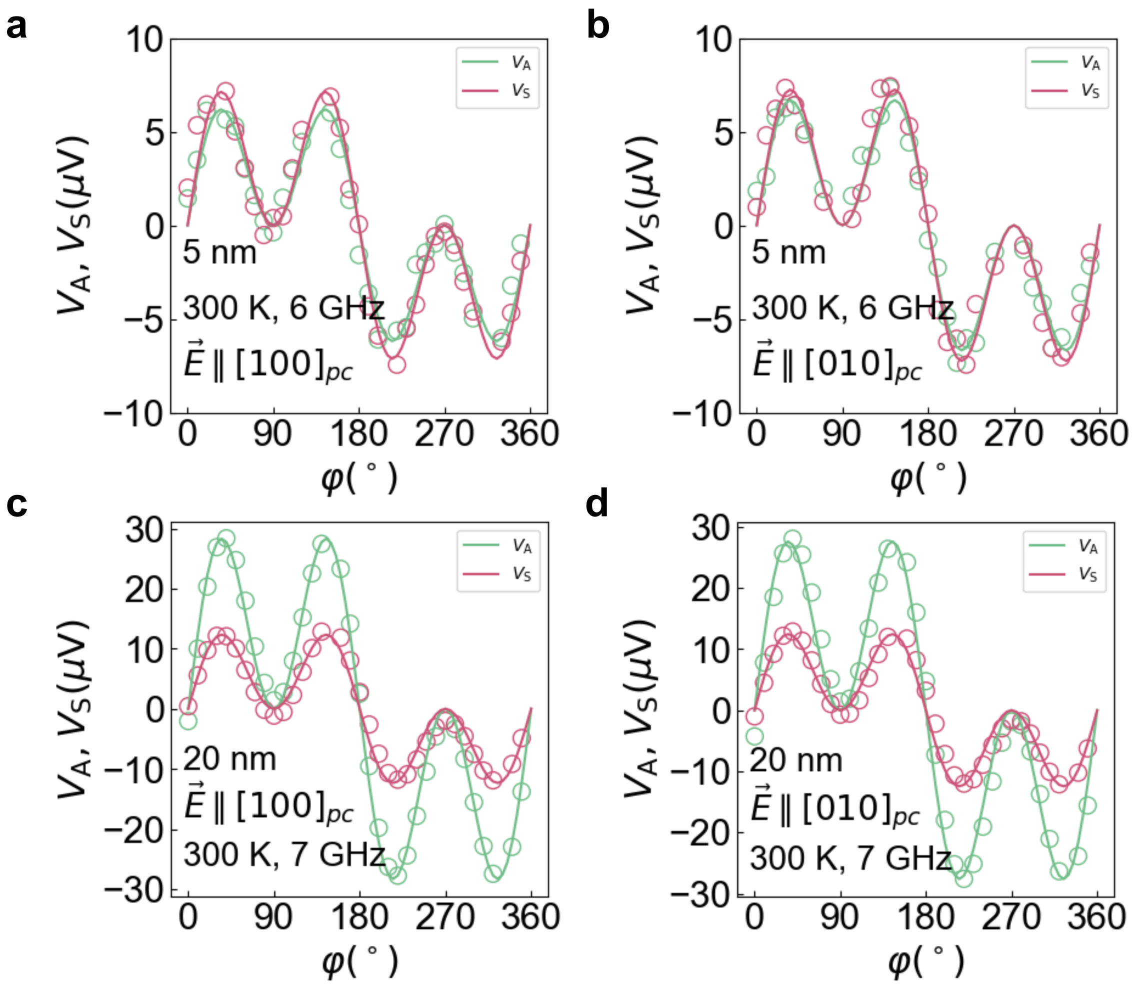

Extended Data Fig. 6. ST-FMR measurements at room temperature for samples $SrRuO_3$ (5, 20 nm)/Py (5 nm). a, b, Anti-symmetric and symmetric components of the mixing voltage for electric fields applied along $[100]_{pc}$ and $[010]_{pc}$ for $SrRuO_3$ (5 nm)/Py (5 nm). The solid curve is a fit to Y component, proportional to $\sin(2\varphi)\cos(\varphi)$. **c, d,** Anti-symmetric and symmetric components of the mixing voltage for electric fields applied along $[100]_{pc}$ and $[010]_{pc}$ for $SrRuO_3$ (20 nm)/Py (5 nm). The solid curve is a fit to Y component, proportional to $\sin(2\varphi)\cos(\varphi)$

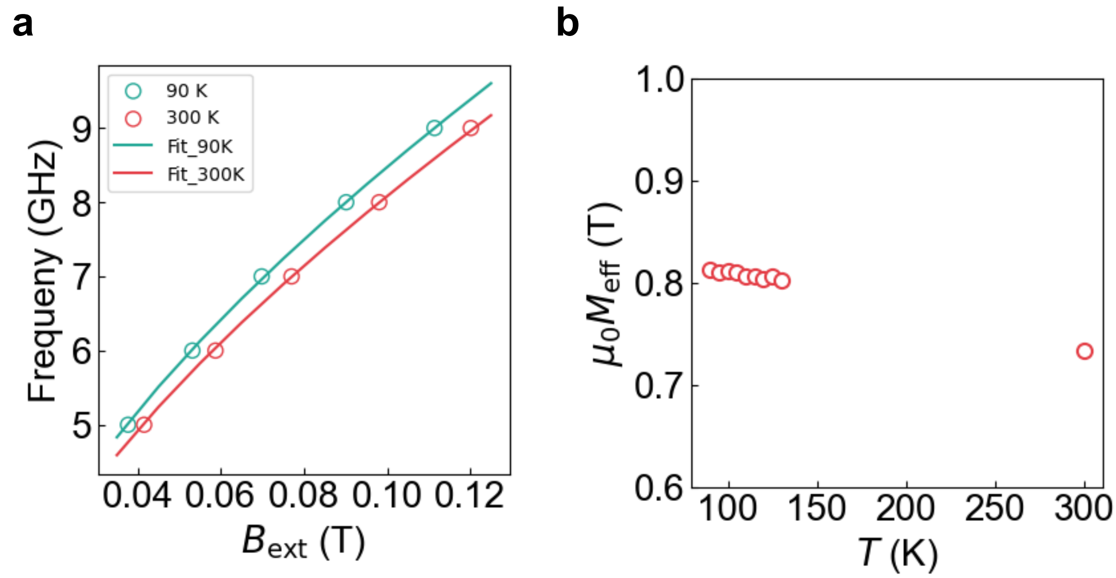

Extended Data Fig. 7. Effective magnetization analysis for sample $SrRuO_3$ (5 nm)/Py (5 nm). a, Measured resonant magnetic fields as a function of frequency at 300 K and 90 K. The solid curves are Kittel fits (to $f = \gamma/2\pi\sqrt{B_{ext}(B_{ext} + \mu_0 M_{eff})}$). **b,** Effective magnetization for $SrRuO_3$ (5 nm)/Py (5 nm) as a function of temperature.

Material	ξ^Z_{DL}	$\sigma^Z_{SH}(\Omega\mathrm{m})^{-1}$	$\rho(\mu\Omega\mathrm{cm})$	ref
Low crystal symmetry				
WTe_2	0.014	3.6×10^3	380	[15]
$MoTe_2$	0.008	1.4×10^3	550	[58]
(114) $MnPd_3$	0.008	14×10^3	60	[17]
$PtTe_2/WTe_2$	0.007-0.032	$(17-25) \times 10^3$	29-154	[59]
Antiferromagnets				
RuO_2	0.008	6×10^3	140	[25]
Mn_3GaN	0.019	8.6×10^3	220	[23]
Ferromagnets				
$[001]_{pc}$ $SrRuO_3$ (20 nm)	0.02 (90 K)	13.9×10^3	143.5	This work

Table 1: A survey of out-of-plane anti-damping torque in various systems for which quantitative measurements have been reported.